Lawrence Berkeley National Laboratory

Title
Approximate solutions for diffusive fracture-matrix transfer: Application to storage of dissolved CO2 in fractured rocks

Permalink
https://escholarship.org/uc/item/2rz3w138

Journal
Water Resources Research, 53(2)

ISSN
0043-1397

Authors
Zhou, Quanlin
Oldenburg, Curtis M
Spangler, Lee H
et al.

Publication Date
2017-02-01

DOI
10.1002/2016wr019868

Peer reviewed

Updated on 12/20/2016

Approximate Solutions for Diffusive Fracture-Matrix Transfer: Application to Storage of Dissolved CO$_2$ in Fractured Rocks

Quanlin Zhou [1], Curtis M. Oldenburg [1], Lee H. Spangler [2], Jens T. Birkholzer [1]

[1] Energy Geosciences Division, Lawrence Berkeley National Laboratory, Berkeley, CA, USA

[2] Big Sky Carbon Sequestration Partnership, Montana State University, Bozeman, MT, USA

Abstract

Analytical solutions with infinite exponential series are available to calculate the rate of diffusive transfer between low-permeability blocks and high-permeability zones in the subsurface. Truncation of these series is often employed by neglecting the early-time regime. In this paper, we present unified-form approximate solutions in which the early-time and the late-time solutions are continuous at a switchover time. The early-time solutions are based on three-term polynomial functions in terms of square root of dimensionless time, with the first coefficient dependent only on the dimensionless area-to-volume ratio. The last two coefficients are either determined analytically for isotropic blocks (e.g., spheres and slabs) or obtained by fitting the exact solutions, and they solely depend on the aspect ratios for rectangular columns and parallelepipeds. For the late-time solutions, only the leading exponential term is needed for isotropic blocks, while a few additional exponential terms are needed for highly anisotropic rectangular blocks. The optimal switchover time is between 0.157 and 0.229, with highest relative approximation error less than 0.2%. The solutions are used to demonstrate the storage of dissolved CO$_2$ in fractured reservoirs with low-permeability matrix blocks of single and multiple shapes and sizes. These approximate solutions are building blocks for development of analytical and numerical tools for hydraulic, solute, and thermal diffusion processes in low-permeability matrix blocks.

1

1. Introduction

Analytical solutions for diffusion in isotropic and anisotropic blocks of low-permeability materials have been fundamental to modeling hydraulic, solute, and thermal diffusion processes in the subsurface [*Carslaw and Jaeger*, 1959; *Crank*, 1975]. These solutions are available for calculating the time-dependent rate of transfer between low-permeability blocks and high-permeability zones, such as generally found in fractured media. For contaminant transport modeling, dominant diffusive transport in low-permeability blocks is coupled with dominant advective and dispersive transport in the high-permeability zones [*Coats and Smith*, 1964; *van Genuchten and Wierenga*, 1976; *Brusseau et al.*, 1989]. This coupling is complicated by simultaneous diffusion in inherently heterogeneous low-permeability blocks of various shapes and sizes in natural unconsolidated aquifers. The simultaneous diffusion can be best represented by multi-rate diffusion models and multi-rate first-order mass-transfer models [e.g., *Haggerty and Gorelick*, 1995; *Willmann et al.*, 2008; *Silva et al.*, 2009]. The complicated coupling, with time-convolution caused by time-dependent mobile-fluid concentrations, has been solved using Laplace transforms for certain flow conditions [*Moench*, 1995; *Haggerty et al.*, 2001], memory functions with recursion [*Carrera et al.*, 1998; *Haggerty et al.*, 2000], or using simpler multi-rate first-order mass transfer with semi-analytical or numerical modeling [*Haggerty and Gorelick*, 1995; *Willmann et al.*, 2008; *Silva et al.*, 2009]. *Haggerty and Gorelick* [1995] showed that a single-rate diffusion model for an isotropic block of given shape and size could be represented equivalently by a multi-rate first-order mass-transfer model with specific capacity ratios and rate coefficients in an infinite series of exponential functions. By this approach, truncation of the infinite series is often employed by neglecting the early-time transfer regime. When only the leading term is used with capacity ratio of 1 (unity) assumed, the mass transfer model is reduced to equivalency with conventional first-order dual-porosity models [*Barenblatt et al.*, 1960; *Warren and Root*, 1963] and with mobile-immobile fluid models [*Coats and Smith*, 1964] that may be accurate for the very late-time regime close to equilibrium [e.g., *Zimmerman et al.*, 1993; *Liu et al.*, 2007; *Guan et al.*, 2008]. Note that modeling approaches for mass transfer in isotropic low-permeability blocks, conceptualized as spheres and cylinders representing soil grains or aggregate soils, and as slabs for clay layers and aquitards, have always assumed locally one-dimensional (1D) diffusion in contaminant transport and remediation studies.

Analytical solutions to 2D and 3D diffusion processes in isotropic and anisotropic rectangular blocks are also available in the literature [*Carslaw and Jaeger*, 1959; *Crank*, 1975; *Holman*, 1990; *Lim and Aziz*, 1995]. These solutions can better represent two and three orthogonal sets of parallel fractures and corresponding matrix blocks in natural fractured reservoirs. However, to our knowledge, all analytical solutions developed for analyzing tracer tests have assumed one set of parallel fractures with single-rate diffusion in the matrix blocks regardless of flow geometry, e.g., for linear flow [*Tang et al.*, 1981; *Sudicky and Frind*, 1982; *Maloszewski and Zuber*, 1985,

1990, 1993], for radial flow [*Becker and Charbeneau*, 2000; *Reimus et al.*, 2003], and for inter-well flow [*Novakowski et al.*, 2004]. Using these analytical solutions, *Zhou et al.* [2006, 2007] analyzed a large number of field tracer tests and estimated apparent single-rate diffusion coefficients. For more complex flow systems, *Carrera et al.* [1998] proposed a hybrid model, with memory functions defined for 1D diffusion, recursion for time-convolution, and numerical modeling of advection-dispersion in fractures. A multi-rate diffusion model was proposed by *Haggerty et al.* [2001] to account for the effect of varying block sizes on the late-time behavior of breakthrough curves (BTCs) measured in a highly fractured dolomite and to interpret the power-law BTCs captured at many sites [e.g., *Hadermann and Heer*, 1996; *Haggerty et al.*, 2000, 2004; *Meigs and Beauheim*, 2000].

The exact analytical solutions for 1D, 2D, and 3D diffusion in low-permeability matrix blocks may exhibit different transfer regimes in the $[0, \infty]$ range of dimensionless time, $T_d = Dt/l^2$, where D is the diffusion coefficient, l is the minimum half-width of a rectangular block or the radius of a cylinder or a sphere, and t is the time. For example, *Carrera et al.* [1998] developed asymptotic solutions for very early times that show $\sqrt{T_d}$ -based behavior, and for very late times after which fractures and the rock matrix are at equilibrium. *Haggerty et al.* [2001] defined a diffusion timescale as $T_d = 1$ after which approximate equilibrium can be assumed for a cubical matrix block. Most recently, *Zhang et al.* [2011] approximated the exact solution for heat loss from a wellbore to the infinite-extent surrounding rock using an early-time solution and a late-time solution separated by a switchover T_d [*Dykhuizen*, 1990]. *March et al.* [2016] approximated the spontaneous counter-current water-oil imbibition flow using an early-time $\sqrt{T_d}$ -based solution that is based on the 1D analytical solution of *McWhorter and Sunada* [1990] and a late-time $\exp(T_d)$ -based solution derived from the exponential solution of *Aronofsky et al.* [1958], with sufficient accuracy compared to high-resolution numerical modeling. The counter-current two-phase flow has also been addressed using multi-rate mass-transfer models for immiscible displacement [*Tecklenburg et al.*, 2013, 2016]. Unified-form approximate solutions with early- and late-time solutions are needed to simplify the exact analytical solutions to 1D, 2D and 3D diffusion in isotropic and anisotropic blocks of low permeability. For example, the exact solution to 3D diffusion in a rectangular parallelepiped at $T_d = 10^{-7}$ (i.e., a very early time) requires a calculation of $1000 \times 1000 \times 1000$ exponential functions, which is computationally expensive.

In this paper, we present unified-form approximate solutions to capture four different regimes that can be defined physically: (1) a very-early-time regime with $\sqrt{T_d}$ -behavior, (2) an early-time regime with $\dfrac{\sqrt{T_d}}{P¿}$)-behavior, where P represents a three-term polynomial function

[*Crank*, 1975], (3) a late-time regime with $\exp(T_d)$ -behavior, and (4) an equilibrium regime in which 99.9% or 99% of the mass has been transferred. Mathematically, the first two regimes can be represented by the early-time solutions, while the last two regimes can be represented by the late-time solutions that are continuous at the switchover T_d with the early-time ones. The unified form of the approximate solutions is developed for isotropic blocks of 1D spherical, cylindrical, and slab-like diffusion, and isotropic and anisotropic rectangular blocks of 2D and 3D diffusion.

For demonstration, we consider the problem of estimating mass transfer between matrix blocks and fractures (or high-permeability zones) in systems relevant to geologic carbon sequestration (GCS), such as fractured reservoirs, coal beds, or fractured cap rock. Specifically, we demonstrate the use of these solutions by calculating the storage efficiency of dissolved CO_2 in fractured reservoirs of very low matrix permeability that are of single and multiple block shapes and sizes. These developed approximate solutions provide a fundamental advance for analytical and numerical modeling of hydraulic, solute, and thermal diffusion in unconsolidated aquifers, fractured reservoirs, coal beds, and cap-rock systems.

2. Approximate Solutions for Diffusive Fracture-Matrix Transfer

2.1. Governing Equation

We are interested in 1D diffusion of dissolved CO_2 (dsCO$_2$) in slab-like, cylindrical, or spherical matrix blocks, 2D diffusion in rectangular columns, and 3D diffusion in rectangular parallelepipeds. The diffusion equation for a matrix block can be written

$$\frac{\partial \phi_m C_r}{\partial t} = \frac{\partial}{\partial x_i}\left(\phi_m D \frac{\partial C_r}{\partial x_i}\right) \tag{1}$$

where ϕ_m is the matrix porosity (i.e., pore volume per unit volume of the matrix), $C_r(x,t)$ is the spatially-varying relative concentration scaled by constant concentration C_0 (i.e., an unchanging solubility limit of dsCO$_2$), t is the time, x_i is the coordinates (¿x,y,z in 3D), and D is the molecular diffusion coefficient in the porous matrix (i.e., the product of tortuosity and diffusion coefficient of dsCO$_2$ in brine). Without loss of generality, it is assumed that the matrix block is saturated with brine and initially free of dsCO$_2$, and the fractures surrounding the block are saturated with aqueous phase and have a constant concentration of C_0 that is fixed with time as a boundary condition. It is also assumed that the matrix porosity and diffusion coefficient are constant in space and time.

To account for fracture-matrix transfer, we further define C_t to be the average concentration in the block at time t, and C_d to be the relative average concentration in the block. If M_t denotes the total amount of diffusing dsCO$_2$ that has entered the block from its bounding fractures at time t, and M_∞ denotes the corresponding quantity after infinite time, we can define a dimensionless mass of dsCO$_2$ as

$$M_d = M_t / M_\infty = C_t / C_0 = C_d \tag{2a}$$

where $M_\infty = \phi_m V C_0$, where V is the volume of the block. M_d can be written in terms of dimensionless time defined by

$$T_d = Dt/l^2 \tag{2b}$$

where l is the half-width of a slab, or the minimum half-fracture spacing of a rectangular column or parallelepiped, or the radius of a cylinder or a sphere.

2.2. Approximate Solutions for Isotropic Matrix Blocks

We are interested in unified-form, approximate solutions to diffusive transfer between a matrix block and surrounding fractures. The exact solutions for spherical, cylindrical, and slab-like blocks are available in *Crank* [1975], and are rewritten in Eqs. (3a), (3b), and (3c) respectively:

$$M_d = 1 - 6 \sum_{n=1}^{\infty} \frac{1}{n^2 \pi^2} \exp\left(-n^2 \pi^2 T_d\right) \tag{3a}$$

$$M_d = 1 - 4 \sum_{n=1}^{\infty} \frac{1}{\beta_n^2} \exp\left(-\beta_n^2 T_d\right) \tag{3b}$$

$$M_d = 1 - 2 \sum_{n=1}^{\infty} \frac{4}{(2n-1)^2 \pi^2} \exp\left(-(2n-1)^2 \pi^2 T_d / 4\right) \ , \tag{3c}$$

where β_n are the positive roots of the Bessel function of the first kind of order zero. Equation (3a-c) can be written in a general form for any isotropic blocks

$$M_d = 1 - \sum_{n=1}^{N} b_{1n} \exp\left(-b_{2n} T_d\right) - \sum_{n=N+1}^{\infty} b_{1n} \exp\left(-b_{2n} T_d\right) \ , \tag{3d}$$

where b_{1n} are the capacity ratios, b_{2n} are the mass-transfer rate coefficients scaled by D/l^2, and $\sum_{n=1}^{\infty} b_{1n}=1$ [*Haggerty and Gorelick*, 1995]. Figure 1a shows the solutions with truncation of various numbers (N) of the exponential terms for spherical and slab-like blocks, indicating that the solutions can be accurate for early-time behavior by keeping a large number of the terms in the infinite series of Eq. (3). For example, $N=1000$ is needed for $T_d=10^{-7}$. For truncation with $N=1,10,25,50$, and 100, we also mark the (M_{dN}, T_{dN}) point as a symbol in Figure 1a to indicate for each N value that the additional contributions from faster diffusion with higher rate coefficients, $\sum_{n=N+1}^{\infty} b_{1n}\exp\left(-b_{2n}T_d\right)$, are negligible in the solutions beyond the time $T_d \geq T_{dN}$. For example, for a slab-like block, we have $T_{dN}=0.213, 0.0030$, 0.00052, 0.00017, or 0.000044 for $N=1,10,25,50$, or 100. Note that all contributions from these faster-diffusion terms are already considered as a part of M_d by their capacity ratios and equilibrium concentrations.

The corresponding solutions for small times are available in *Crank* [1975] and rewritten respectively for a spherical, cylindrical, and slab-like block, respectively:

$$M_d=\frac{6}{\sqrt{\pi}}\sqrt{T_d}+12\sqrt{T_d}\sum_{1}^{\infty} ierfc\left(n/\sqrt{T_d}\right)-3T_d \tag{4a}$$

$$M_d=\frac{4}{\sqrt{\pi}}\sqrt{T_d}-T_d-\frac{1}{3\sqrt{\pi}}\left(T_d\right)^{3/2}+\dots \tag{4b}$$

$$M_d=\frac{2}{\sqrt{\pi}}\sqrt{T_d}+4\sqrt{T_d}\sum_{1}^{\infty}\left(-1\right)^{n} ierfc\left(n/\sqrt{T_d}\right) , \tag{4c}$$

where *ierfc*() is the integral complementary error function.

Based on the exact solutions in Eq. (3) and the solutions for small times in Eq. (4), we develop approximate solutions by keeping only the leading term ($N=1$) in the infinite series of the exact solutions for large times, and by keeping the first three terms written in terms of $\sqrt{T_d}$ for small times. We introduce the switchover dimensionless time (T_{d0}) between the early and late times so that the solutions are continuous in the time domain. The developed approximate solutions for a spherical, cylindrical, and slab-like block have the unified form:

$$M_d = \begin{cases} a_1\sqrt{T_d} + a_2 T_d + a_3 (T_d)^{3/2} & T_d \leq T_{d0} \quad (5a) \\ 1 - \sum_{j=1}^{N} b_{1j}\exp[-b_{2j}T_d], & T_d > T_{d0} \quad (5b) \end{cases}$$

where a_1 , a_2 , a_3 , b_{1j} , b_{2j} are coefficients with different values for the different shapes of blocks, and N is the number of leading exponential terms in the exact solutions. All the coefficients for the three shapes of an isotropic block are listed in Table 1, where β_1 (2.4048255577) is the first root of the Bessel function of the first kind of order zero.

To determine T_{d0} for each block shape, we calculate the relative errors for 402 T_d data points between 0 and 0.4, with an increment of 0.001. As shown in Figure 1b, the first relative error is between the exact solutions in Eq. (3) using $N=1000$ and the approximate solution in Eq. (5a), while the second relative error is between Eq. (3) and Eq. (5b), both relative to the exact solutions for all T_d data points. The first relative error increases with T_d , while the second one decreases. By comparing these two relative errors, we determine the optimal T_{d0} at which the two relative errors are equal, minimizing the maximum relative error over the entire time domain. Note that *a-priori* T_{d0} is not needed in the determination of T_{d0} . As a result, the faster-diffusion terms with higher rate coefficients have negligible time-dependent impact on the late-time solutions as their contributions are already considered in M_d during the early times.

The relative errors in percentage of the exact solutions are less than 0.15% and 0.03% for a slab and sphere, respectively. For a cylindrical block, the highest relative error is 0.47% at $T_{d0}=0.123$ when using $a_2=-1$ and $a_3=1/(3\sqrt{\pi})$ from Eq. (4b); to reduce the relative error, we fit a_2 and a_3 against the exact solutions at 109 logarithmically-spaced points of T_d in the range [$10^{-5}, 0.2$], while keeping $a_1=4/\sqrt{\pi}$. The obtained values of a_2 and a_3 are listed in Table 1, with the maximum relative error reduced to less than 0.1%.

The obtained values of T_{d0} for the three shapes of an isotropic block are also listed in Table 1, along with the maximum relative errors (ε_{max}) of the approximate solutions, the dimensionless mass, $M_{d0}=M_d\big|^{T_{d0}}$), at T_{d0} , and the dimensionless area-to-volume ratio ($R=Al/V$) scaled by *l*, where *A* is the fracture-matrix interface area for a block.

As shown in Figure 1c, the approximate solutions are in excellent agreement with the exact solutions (calculated using finite *N* = 1000 for spheres and slabs or $N=150$ for cylinders) over the range of $T_d=[10^{-5},10]$ for spherical, cylindrical, and slab-like blocks. It is also

shown that the leading-term solutions are sufficiently accurate for the late-time behavior for $T_d > T_{d0}$.

T_{d0} is relatively large, between 0.157 and 0.213, and is far longer than the arrival times of concentration fronts at the block center, as shown by $C_r(x,t)$ in Figure 1d. At T_{d0}, the relative concentration at the block center is 0.25 and 0.58, and the dimensionless mass is 0.52 and 0.87 for a slab and sphere, respectively. This indicates that the early-time behavior of diffusion accounts for more than 50% dsCO$_2$ mass storage in fractured rock and is accurately modeled by the three-term polynomial functions in terms of $\sqrt{T_d}$ in Eq. (5a). After T_{d0}, the dimensionless mass follows the exponential function with a decreased flow rate with time for additional storage. The dimensionless time, T_{de}, needed to reach equilibrium (defined here by $M_d \geq 0.99$) is 1.91, 0.76, and 0.44 for a slab-like, cylindrical, and spherical block, respectively.

2.3. Approximate Solutions for Anisotropic Matrix Blocks

A slab block can be formed by one set of two parallel fractures with fracture spacing of $2l$. Two orthogonal sets of parallel fractures with fracture spacing of 2 l_x and 2 l_y can form a rectangular-column block and three orthogonal sets of parallel fractures with fracture spacing of $2l_x$, $2l_y$, and $2l_z$ can form a rectangular-parallelepiped block. Here we introduce $l = l_x \leq l_y$ or $l = l_x \leq l_y \leq l_z$, and the aspect ratios $R_{li} = l/l_i, i = y, z$, where x, y, z are the local coordinates and may not be the same as the global ones.

For a block of a rectangular column, the analytical solution for M_d can be derived by taking the product of the dimensionless solution for a slab-like block in Eq. (3c) [*Carslaw and Jaeger*, 1959; *Crank*, 1975; *Holman*, 1990; *Lim and Aziz*, 1995], and is rewritten here in terms of aspect ratio R_{ly}:

$$M_d = 1 - \left(\frac{8}{\pi^2}\right)^2 \sum_{n_x=1}^{\infty} \sum_{n_y=1}^{\infty} \frac{1}{(2n_x-1)^2 (2n_y-1)^2} \exp\left[-\left((2n_x-1)^2 + (2n_y-1)^2 R_{ly}^2\right)\frac{\pi^2}{4} T_d\right]. \quad (6)$$

There are no analytical solutions for early- and late-time regimes available in the literature. We assume that the solution form in Eq. (5a) remains valid for the early-time solutions of a rectangular-column block. Coefficient a_1 solely depends on the dimensionless area-to-volume ratio; when scaling/dividing by R, the very-early-time solutions (e.g., $T_d \leq 10^{-4}$ with a penetration depth of 0.04 l with 0.5% concentration) in Eq. (5a) are independent of block geometry [*Carrera et al.*, 1998], as shown in Table 1.

To determine coefficients a_2 and a_3, we select 11 values of aspect ratio R_{ly} in the range [0, 1] with an increment of 0.1. For each R_{ly} value, we calculate the exact solution at 201 points of T_d that are logarithmically-spaced between 10^{-7} and 10 using Eq. (6) and $N_x \times N_y = 2000 \times 2000$. The first 159 data points (up to $T_d = 0.21$) are used to fit the three coefficients (a_1, a_2, a_3) simultaneously. The goodness of each fit is 1.0, indicating that Eq. (5a) has the exact form of solutions, with the coefficients estimated accurately. It is found that a_1 and a_2 are linearly corrected with R_{ly}, while a_3 is negligible, for the 11 datasets. The initial fitting of each dataset is refined by fixing $a_1 = 2(1+R_{ly})/\sqrt{\pi}$ and $a_3 = 0$ and by only fitting a_2; the sum of the square of residual difference between the exact and approximate solutions is less than 5×10^{-7}. The obtained values of coefficient a_2 are then perfectly fitted as a linear function of R_{ly} (see Figure 2b). Note that the fitting of coefficient a_2 is not sensitive to T_{d0} as long as it is between 0.21 and 0.23.

For the late-time approximate solutions, the leading-term approximation may not be sufficiently accurate. If the degree of anisotropy increases and R_{ly} decreases, a few additional exponential terms in Eq. (6) are needed. Therefore, the coefficients for both early- and late-time approximate solutions in Eq. (5) for rectangular columns are written

$$a_1 = 2(1+R_{ly})/\sqrt{\pi} \quad , \quad a_2 = -1.2735\, R_{ly} \quad , \quad a_3 = 0 \quad , \tag{7a}$$

$$b_{1\,j} = \left(\frac{8}{\pi^2}\right)^2 / \left((2n_{xj}-1)^2 (2n_{yj}-1)^2\right) \quad , \tag{7b}$$

$$b_{2\,j} = \frac{\pi^2}{4} c_j \quad ; \quad c_j = (2n_{xj}-1)^2 + (2n_{yj}-1)^2 R_{ly}^2 \tag{7c}$$

and the number of exponential terms ($j = 1, N$) needed in Eq. (5b) can be determined practically by

$$c_j \le 11 \quad \text{with} \quad b_{1\,j} \exp\left(-b_{2\,j} T_{d0}\right) > tol \,, \tag{7d}$$

where tol is a cutoff, depending on the degree of anisotropy. $tol = 5 \times 10^{-4}$ for $R_{ly} > 0.1$, while $tol = 1 \times 10^{-4}$ is needed for $R_{ly} \le 0.1$ to control the relative error below 0.5% for $R_{ly} = 0$. This means all the N terms kept for late-time calculations have small rate coefficients and high accuracy. N depends on the aspect ratio R_{ly} (see Figure 2b). $N \le 2$ is sufficient for $R_{ly} \ge 0.6$, while $3 \le N \le 6$ is needed for $0.2 \le R_{ly} < 0.6$. $N = 17$ is needed for $R_{ly} = 0.05$ because of the slow convergence of the exact solution in

Eq. (6). Note that $\frac{8}{\pi^2}\sum_{n_y=1}^{\infty}\frac{1}{(2n_y-1)^2}=1$ and $N=32$ when $R_{ly}=0$. Practically, all terms meeting Eq. (7d) when using $N_x \times N_y = 100 \times 100$ in Eq. (6) are used for late-time calculations.

As shown in Figure 2a, the approximate solutions for the early- and late-time regimes are in excellent agreement with the exact solutions obtained with $N_x \times N_y = 2000 \times 2000$ in Eq. (6) for the range $0 \leq R_{ly} \leq 1$. It is also shown that the linear effect of the aspect ratio R_{ly} on the solutions is significant and cannot be neglected for an anisotropic rectangular-column block.

Similarly, for a block of a rectangular parallelepiped, the following exact solutions can be written [*Lim and Aziz*, 1995]:

$$M_d = 1 - \left(\frac{8}{\pi^2}\right)^3 \sum_{n_x=1}^{\infty}\sum_{n_y=1}^{\infty}\sum_{n_z=1}^{\infty} \frac{1}{(2n_x-1)^2(2n_y-1)^2(2n_z-1)^2}$$
$$\exp\left[-\left((2n_x-1)^2+(2n_y-1)^2 R_{ly}^2+(2n_z-1)^2 R_{lz}^2\right)\frac{\pi^2}{4}T_d\right]. \tag{8}$$

In the case of an anisotropic rectangular parallelepiped with $l_x \neq l_y \neq l_z$, it is assumed that Eq. (5a) is still valid for the early-time approximate solutions and Eq. (5b) is valid for the late-time approximate solutions. Again, coefficient a_1 is determined by the dimensionless area-to-volume ratio (see Table 1). To determine coefficients a_2 and a_3, we first calculate the exact solutions using Eq. (8) for a number of (R_{ly}, R_{lz}) pairs, with an increment of 0.1 and $0 \leq R_{ly} \leq 1$ and $0 \leq R_{lz} \leq R_{ly}$. The exact solutions are calculated using $N_x \times N_y \times N_z = 1000 \times 1000 \times 1000$ for the 201 logarithmically-spaced points of T_d over $[10^{-7}, 10]$. We then fit the first 159 data points to the early-time solution in Eq. (5a) with assumed $T_{d0}=0.21$ for each (R_{ly}, R_{lz}) pair to estimate these coefficients; the goodness of these 66 fits is all higher than 0.9999, indicating that the solution form in (5a) works exactly as assumed. We finally fit the 66 values of coefficients a_2 and a_3 (see Figure 3a and 3b) and obtain their relationships with the aspect ratios R_{ly} and R_{lz} in Eqs. (9b) and (9c). As shown in Figure 3c, the maximum relative errors of the early-time approximate solutions at $T_{d0}=0.22$ for the 66 cases are all small, less than 0.12%.

For the late-time approximate solutions, the leading term is less than 0.1% higher than the exact solution at $T_{d0}=0.22$ for the isotropic case with $R_{ly}=R_{lz}=1$, while it is 33% higher for the highly anisotropic case with $R_{ly}=R_{lz}=0$. Different tol values are used for different degree of block anisotropy: $tol=5\times10^{-4}$ is used for $R_{ly} \geq R_{lz} \geq 0.2$, while $tol=1\times10^{-5}$ is used

for $R_{ly} \geq R_{lz} = 0$. As a result, the number of exponential terms (N) needed depends on the aspect ratios R_{ly} and R_{lz} (see Figure 3d). In this way, the maximum relative error of the late-time approximate solutions is less than 0.2% for all the 66 cases.

The solution coefficients in Eq. (5) for a rectangular parallelepiped are written:

$$a_1 = 2(1 + R_{ly} + R_{lz})/\sqrt{\pi} \tag{9a}$$

$$a_2 = -1.2735\,R_{ly} - 1.2645\,R_{lz} - 1.2791\,R_{ly}\,R_{lz} \tag{9b}$$

$$a_3 = 1.4232\,R_{ly}\,R_{lz} \tag{9c}$$

$$b_{1j} = \left(\frac{8}{\pi^2}\right)^3 / \left((2n_{xj}-1)^2(2n_{yj}-1)^2(2n_{zj}-1)^2\right) \tag{9d}$$

$$b_{2j} = \frac{\pi^2}{4}c_j \; ; \; c_j = \left((2n_{xj}-1)^2 + (2n_{yj}-1)^2 R_{ly}^2 + (2n_{zj}-1)^2 R_{lz}^2\right) \tag{9e}$$

and N is determined by Eqs. (7d) and (9e).

Figure 2c shows excellent agreement between the exact solutions in Eq. (8) and the approximate solutions in Eq. (5) with solution coefficients in Eq. (9) for the 66 (R_{ly}, R_{lz}) pairs of a rectangular-parallelepiped block. The excellent agreement indicates that we have correct solution forms in Eq. (5a) for the early-time regime and Eq. (5b) for the late-time regime. The effect of aspect ratios R_{ly} and R_{lz} is significant for the transitions from 1D diffusion in a slab-like block to 2D diffusion in a rectangular-column block then to 3D diffusion in a rectangular-parallelepiped block.

For a block of an isotropic rectangular column (i.e., square column) and an isotropic rectangular parallelepiped (i.e., cube), we employ the exact solutions in Eqs. (6) and (8), respectively, and the approximate solutions in Eq. (5) with $N=1$, and derive coefficients a_2 and a_3 in the same procedures presented above. The derived coefficients for cubical and square-column blocks are listed in Table 1. Note that the coefficients for a cube (or a square column) in Table 1 are consistent with the values calculated using Eq. (9b-c) with $R_{ly} = R_{lz} = 1$ (or Eq. (7a) with $R_{ly} = 1$).

The determination of exact T_{d0} for square columns or cubes follows the same method presented for the isotropic blocks with 1D diffusion, and is shown in Figure 1b. $T_{d0} = 0.229$ is

obtained for cubes and $T_{d0}=0.215$ for square columns, which are close to $T_{d0}=0.213$ for slabs. Note that *a-priori* T_{d0} (=0.21) is used in the fitting of (a_2, a_3), but not used in determining T_{d0}. However, the slight difference between the exact and *a-priori* T_{d0} is found to have no effect on the estimated (a_2, a_3) values. As shown in Figure 2, the solution for an anisotropic rectangular column with any R_{ly} is between those of a square column and a slab. The approximation error by the *N*-term truncation is less than 0.06% based on Eqs. (6) and (7c-d). For the 11 R_{ly} values, the relative error at $T_{d0}=0.22$ varies from 0.073% to 0.164% for the early-time solutions, and varies from 0.046% to 0.115% for the late-time solutions (see Figure 1b). For an anisotropic rectangular parallelepiped, the solution with any R_{ly} and R_{lz} is between those of a cube and a slab, and the approximation error by the *N*-term truncation is less than 0.06% based on Eqs. (7d), (8), and (9e). Similarly, for the 66 (R_{ly}, R_{lz}) values, the relative error at $T_{d0}=0.22$ is also very small for the early-time and late-time solutions. As a result, $T_{d0}=0.22$ is used for any anisotropic rectangular columns or parallelepipeds, with the maximum relative error less than 0.2% (see Table 1).

For all isotropic blocks (e.g., spherical, cylindrical, slab-like, square-column, and cubical), the unified form of approximate solutions in Eq. (5) with their coefficients in Table 1 can be used for modeling diffusive fracture-matrix transfer. As shown in Figure 2d, the difference between spherical and cubical solutions and between cylindrical and square-column solutions is small and can be attributed to the small difference in their coefficients a_2, a_3, b_1 and b_2. We suggest using the correct block shape for modeling, in particular for fractured rocks. For an isotropic slab, it is more computationally efficient to use Eq. (5) with slab coefficients than using an anisotropic rectangular-column block with $R_{ly}=0$ or an anisotropic rectangular-parallelepiped block with $R_{ly}=\dot\iota$ $R_{lz}=0$. For the latter, a larger number of additional exponential terms are needed to achieve the same accuracy as the leading term only in the former because the convergence of $\dfrac{8}{\pi^2}\displaystyle\sum_{n=1}^{\infty}\dfrac{1}{(2n-1)^2}=1$ is slow (see Figure 3d).

2.4. Fracture-Matrix Transfer Flux

As discussed above, by neglecting the higher-order terms in Eq. (5a) at very early times, we have

$$M_d=2R\sqrt{T_d}/\sqrt{\pi}, T_d\leq T_{d1} \tag{10}$$

where T_{d1} is the very-early dimensionless time cutoff, below which the $\sqrt{T_d}$-behavior of the dimensionless mass remains valid. T_{d1} can be 0.001 for high-accuracy modeling, while $T_{d1}=0.01$ is sufficiently good in some cases. In the case $T_d\leq T_{d1}$, the dimensionless mass depends only on the dimensionless area-to-volume ratio, and is independent of the block shape.

Later on, the dimensionless mass is affected by the geometry and volume of the block because $dsCO_2$ migration and distribution depend on the no-flow condition at the block center. For example, *Carrera et al.* [1998] used this very-early-time solution. They also defined an asymptotic solution for very late times, $T_d \geq T_{de}$, in which the matrix is at equilibrium with the surrounding fractures. In this case, the effect of the rock matrix is considered by using a retardation factor (i.e., the ratio of matrix to fracture porosity) [*Malozewski and Zuber*, 1985].

In summary, four flow regimes can be defined using the three dimensionless times, T_{d1}, T_{d0}, and T_{de} : (1) the very-early-time $\sqrt{T_d}$ -behavior regime, (2) the early-time $\frac{\sqrt{T_d}}{P}$¿)-behavior regime, where P is the three-term polynomial function in Eq. (5a), (3) the late-time $\exp(T_d)$ -behavior regime shown in Eq. (5b), and (4) the equilibrium regime. Mathematically, the first two regimes can be represented by the early-time solutions in Eq. (5a), and the last two regimes can be represented by the late-time solutions in Eq. (5b).

For a given block i of known shape and characteristic size l_i, the fracture-matrix mass flowrate, f_i, for a unit concentration and brine density in fractures per unit volume of the block, can be written

$$f_i = \frac{d M_{di}}{dt} = \frac{D}{l_i^2} \frac{d M_{di}}{dT_{di}},$$ (11a)

with the derivative for block i expressed using the approximate solutions in Eq. (5):

$$\frac{d M_{di}}{dT_{di}} = \begin{cases} a_1/\left(2\sqrt{T_{di}}\right) + a_2 + \frac{3}{2} a_3 \sqrt{T_{di}}, T_{di} \leq T_{d0i} \\ ¿ \sum_{j=1}^{N} b_{1ji} b_{2ji} \exp\left(-b_{2ji} T_{di}\right), T_{di} > T_{d0i} \end{cases}$$ (11b)

Let us examine the fracture-matrix mass flowrate, F, per unit volume of fractured media, with volume fractions ϕ_f and $1-\phi_f$ for the fractures and the rock matrix, respectively. It is assumed that the unit-volume fractured medium consists of *K* blocks of different shapes and different sizes, with a characteristic half-width l_i and volume fraction $w_i, i=1, K$, as well as different intrinsic matrix porosity ϕ_{mi}. The total mass of $dsCO_2$ stored in these blocks per unit volume of fractured media at time *t* is

$$W(t)=(1-\phi_f)\rho_b C_0 \sum_{i=1}^{K} \phi_{mi} w_i M_{di} \quad ; \quad T_{di}=Dt/l_i^2 \quad , \tag{12}$$

where ρ_b is the brine density. The mass flux between surrounding fractures and these blocks per unit volume of fractured media is

$$F(t)=\frac{dW}{dt}=(1-\phi_f)\rho_b C_0 \sum_{i=1}^{K} \phi_{mi} w_i f_i \quad , \tag{13}$$

2.5. Comparison to Single-Rate First-Order Dual-Porosity Models

The mass transfer flux for the first-order dual-porosity model for fractured rocks can be written in terms of the relative average concentration (C_d) in a block and the relative fracture concentration C_f ¿ $\overset{\text{¿}1}{}$ in our constant-concentration demonstration case):

$$f=-\alpha(C_d-C_f)=d\,C_d/dt\,, \tag{14a}$$

where α is the first-order rate coefficient. For an isotropic block of a given shape listed in Table 1, using Eq. (11) for the late-time solution with $N=1$, we have

$$\alpha=b_2\,D/l^2 \tag{14b}$$

Using the initial condition $C_d=M_d=0$ at $t=T_d=0$, we have from Eq. (14a)

$$C_d=M_d=1-\exp(-\alpha t)=1-\exp(-b_2 T_d) \tag{14c}$$

Note that the first-order dual-porosity model in Eq. (14c) has a single rate coefficient b_2 (normalized by D/l^2) and a full capacity ratio ($b_1=1$) acting in the entire time domain. This is different from the late-time approximate solutions in Eq. (5b) in which coefficient b_1 ($¿1$) represents the capacity ratio for the rate coefficient b_2 , as shown by *Haggerty and Gorelick* [1995]. In our late-time approximate solutions, $1-b_1$ corresponds to faster mass-transfer rates and equilibrium behavior whose effects are already included through the early-time solutions on M_d . Moreover, the first-order model is not accurate for the early-time regime because it has T_d -behavior, rather than the correct $\sqrt{T_d}$ -behavior at very early times. Therefore, the first-order dual-porosity model is accurate only in the equilibrium regime when the b_1 effect disappears.

For a moderately anisotropic rectangular column or parallelepiped, Eq. (14) works for the first-order models, as long as only the leading term is needed ($N=1$) for the late-time approximate solutions. For a highly anisotropic block, $N>1$ and a multi-rate first-order model with $\alpha_j = b_{2j} D/l^2$ may be needed to account for the effect of strong anisotropy, as has done for the effect of varying sizes of isotropic blocks [*Haggerty and Gorelick*, 1995; *Haggerty et al.*, 2001; *Willmann et al.*, 2008; *Silva et al.*, 2009].

Figure 4 shows the comparison between the conventional first-order dual-porosity models with the optimal α values in Eq. (14b) and our approximate solutions for a slab-like block and a cubical block . To show the effect of the different single-rate α values or shape-factor values that have been used in petroleum engineering [*Warren and Root*, 1963; *Kazemi et al.*, 1976; *Coats*, 1989; *Lim and Aziz*, 1995], we include a case with geometry-based $\alpha = RD/l^2$ in the first-order dual-porosity model. The dual-porosity models significantly underestimate M_d at both early and late times. The dual-porosity model with optimal α only accurately predicts the time needed to reach the equilibrium, while the dual-porosity model with the geometry-based α predicts a much longer equilibrium time. For petroleum engineering, the shape factor (σ) is related to the dimensionless area-to-volume ratio via $\sigma = R$. Numerically, the mass transfer flux can be written using the nodal distance, d, from fractures:

$$f = \frac{DA}{V}\frac{C_d - C_f}{d} = DR\frac{C_d - C_f}{ld} \quad \text{, and} \quad d = \frac{\overset{R}{\dot{\iota}}}{\underset{\dot{\iota}}{b_2}} \tag{14d}$$

For an isotropic slab-like, square-column, or cubical block, $d = \dfrac{\overset{4}{\dot{\iota}}}{\underset{\dot{\iota}}{\dfrac{\pi^2}{\dot{\iota}\dot{\iota}l}}}$, shorter than the half-width

from the fracture to the block center. For a spherical block, $d = \dfrac{\overset{3}{\dot{\iota}}}{\underset{\dot{\iota}}{\dfrac{\pi^2}{\dot{\iota}\dot{\iota}l}}}$. These *d* values are useful to guide numerical discretization to represent the gradients of dsCO$_2$ concentration.

Different improvements have been made for conventional dual-porosity models, including the multiple interacting continuum (MINC) model by further dividing a block into nested sub-

elements [*Pruess and Narasimhan*, 1985], and nonlinear fracture-matrix transfer equations using specific analytical solutions [e.g., *Dykhuizen*, 1990; *Zimmerman et al.*, 1993]. Macroscopic models based on the Continuous Time Random Walk (CTRW) framework were developed to characterize the interaction between the fractured and porous rock domains using a probability distribution function of residence times [*Cortis and Birkholzer*, 2008; *Geiger et al.*, 2010]. The best improvement is the multi-rate first-order mass transfer models that are compatible with the conventional dual-porosity model concept. These models have been implemented in some existing advection-dispersion transport simulators [*Haggerty and Gorelick*, 1995; *Carrera et al.*, 1998; *Haggerty et al.*, 2001; *Willmann et al.*, 2008; *Silva and Carrera*, 2008; *Silva et al.*, 2009]. The approximate solutions developed here can be used as building blocks within the framework of the existing multi-rate mass transfer or multi-rate diffusion models. The demonstration of this coupling is beyond this short technical report of methods.

3. Application Examples of Storage of Dissolved CO_2 in Fractured Reservoirs

Estimating mass transfer between matrix blocks and fractures (or high-permeability zones) is important for GCS in fractured reservoirs, e.g., fractured carbonate reservoirs, in coal beds, or in cap rocks with fractures. For demonstration of the new solutions, we present here mass transfer calculations related to supercritical CO_2 ($scCO_2$) injection into fractured reservoirs with low matrix permeability, high matrix entry capillary pressure, and high matrix porosity. In this scenario, injected $scCO_2$ migrates through the fracture network, and dissolves at the interfaces between fractures and matrix blocks. There is no $scCO_2$ in the rock matrix blocks because of their high gas-entry (capillary) pressure and low permeability. The low fracture porosity produces a large CO_2 plume in the fracture network and thus large interfacial areas between fractures and the rock matrix that is available for diffusive mass flux of $dsCO_2$ into the matrix. In the matrix blocks, only diffusion of $dsCO_2$ occurs. The storage capacity of fractured reservoirs can be large and the storage efficiency can approach with time a mass-fraction solubility that ranges from 2% to 6% depending on the salinity of resident brine and pressure and temperature [*Spycher et al.*, 2003; *Spycher and Pruess*, 2005]. This mass storage efficiency is similar to or higher than the value for porous sandstone reservoirs at a regional scale where the effect of various $scCO_2$ efficiency factors and pressure buildup constraints apply [*USDOE*, 2008; *Zhou et al.*, 2008, 2009, 2010; *Birkholzer et al.*, 2015]. The key question we address here is the time scale needed to reach solubility limits in the rock matrix for various block shapes and sizes or fracture spacing in the three dimensions.

For the fractured rock system in the scenario of interest, there is no $scCO_2$ or $dsCO_2$ initially in the system. Injected $scCO_2$ migrates through the fractures and simultaneously dissolves into the aqueous phase at the fracture-matrix interfaces. It is assumed that the $scCO_2$ dissolution is

instantaneous at these interfaces with a concentration at the solubility limit under the local conditions of pressure, temperature, and salinity. It is also assumed that the concentration at these interfaces can be maintained at the solubility limit during continuous scCO$_2$ injection because of high fracture flow rate of injected scCO$_2$. Once scCO$_2$ migrates to a given matrix block, the diffusion of dsCO$_2$ from its surrounding fractures to this block will continue until a full equilibrium concentration of dsCO$_2$ is achieved. Two examples are employed to demonstrate the application of the developed approximate solutions to modeling diffusive fracture-matrix transfer of dsCO$_2$ for solubility trapping in a fractured reservoir system.

3.1. Example 1 for Block-Scale Modeling

In the first example, we are interested in local diffusion processes in a unit pore volume of fractured matrix that consists of blocks of single shape and size or a mixture of blocks of different sizes. Three cases of single-size blocks are considered, including (1) slabs, (2) cubes, or (3) rectangular parallelepipeds with $R_{ly}=0.5$ and $R_{lz}=0.2$. In the last case, four cubical blocks with half-fracture spacing of l, $2l$, $3l$, and $6l$ and their volumetric fractions of 0.42, 0.24, 0.17 and 0.17 respectively are considered [*Haggerty and Gorelick*, 1995]. In each case, the characteristic minimum half-fracture spacing varies from 0.01 m to 3.0 m and the matrix diffusion coefficient is assumed to be $D=2\times10^{-10}$ m^2/s. We use the developed approximate solutions to calculate the dimensionless mass from 0 to 100 years.

Figure 5a-c shows the contours of dimensionless mass as functions of minimum half-fracture spacing and the time for the three cases of single-size blocks. It can be seen that for a given *l*, cubical blocks are more effective than the rectangular-parallelepiped blocks that are in turn more effective than the slab-like blocks for storage of dsCO$_2$. For $l=1$ m, the dimensionless mass is 0.63, 0.77, and 0.95 for the cases of slabs, rectangular parallelepipeds, and cubes at 50 years, while it is 0.83, 0.92, and 0.995 at 100 years, respectively. This means that for densely fractured reservoirs with the minimum half-fracture spacing less than 1.0 m, the time scale needed to reach the solubility limit in the rock matrix is comparable with or less than the lifetime of a GCS project, and the storage of dsCO$_2$ in fractured reservoirs is effective, with a storage efficiency of 2-6% mass fraction. Figure 5d shows the comparison of the time-dependent dimensionless mass for the multi-block case and single-block cases of cubes and rectangular parallelepipeds for $l=0.25, 0.5, 1.0$ m. The multi-block case shows a more gradual increase in M_d with time because of the effects of blocks of large half-spacing.

3.2. Example 2 for Reservoir-Scale Modeling

In this example, we are interested in the storage of dsCO$_2$ in a fractured reservoir that is $B=20$ m thick. The in situ reservoir pressure is 152 bar, the temperature is 59 °C, the salt mass fraction is 0.093 with mole fraction of 1.75 molal, and the brine density is $\rho_b=¿$ 1053 kg/m^3. The fracture porosity is $\phi_f=0.5$ and fracture permeability is high so that the pressure

effect on fluid densities is small. The intrinsic matrix porosity is $\phi_m = 0.20$ and matrix permeability is very small so that no scCO$_2$ is in the rock matrix. The scCO$_2$ density under the injection conditions is $\rho_{CO2} = ¿$ 623 kg/m^3 and the solubility limit of dsCO$_2$ mass fraction in brine is calculated to be $C_0 = ¿$ 0.032. For simplicity, we assume scCO$_2$ flow in the reservoir is 1D radial flow with a piston front of scCO$_2$. Diffusion of dsCO$_2$ from fracture-matrix interfaces into matrix blocks is considered as the sink for scCO$_2$ in fractures.

The mass balance equation for injection time t can be written

$$\int_0^t Q d\tau = \int_0^{R(t)} 2\pi \phi_f \rho_{CO2} rBdr + \int_0^{R(t)} 2\pi(1-\phi_f)\phi_m \rho_b C_0 M_d(r,t) rBdr \qquad (15)$$

where $R(t)$ is the radius of the scCO$_2$ plume from the injection well, and Q is the total scCO$_2$ injection rate. To simplify the calculation, we use a constant injection rate of 16 kg/s to maintain the scCO$_2$ plume in fractures, i.e., the first term on the right-hand side of Eq. (15). We add the time-dependent injection rate to account for the mass of dsCO$_2$ stored in the rock matrix, i.e., the second term in Eq. (15). The total injection rate is the combination of the constant rate of 16 kg/m^3 for scCO$_2$ storage in fractures and the time-dependent rate for dsCO$_2$ storage in the rock matrix. We use the constant injection rate to track the scCO$_2$ front and to determine the start time of dsCO$_2$ diffusion into the rock matrix at the scCO$_2$ front. The dimensionless mass (M_d) in this case is relevant to the dsCO$_2$ mass stored in the rock matrix that is in contact with scCO$_2$ in fractures. The time-step size for the calculation is 0.02 year and is uniform over a total of 100 years of injection, leading to 5000 time steps.

Three cases for the rock matrix are considered: (1) single-size cubes, (2) a mixture of four cubes of different sizes, and (3) single-size rectangular parallelepipeds with $R_{ly} = 0.5$ and $R_{lz} = 0.2$. All parameters of these blocks are the same as in Example 1. Computationally, $T_{de} = 4.0$ for the third case which cuts off the regions with equilibrium dsCO$_2$ mass fraction so that no calculation is needed for them.

Figure 6a-c shows the profiles of dsCO$_2$ dimensionless mass in the rock matrix at different injection times for the three cases of matrix blocks, each with three scenarios of $l = 0.25, 0.50, 1.0$ m. For the single-size-cube rock matrix, it only takes 6 years for a block to reach equilibrium ($M_d > 0.99$) in the scenario of $l = 0.25$ m. For a long-term injection, the majority of the volume of the rock matrix in contact with scCO$_2$ in fractures is at the solubility limit, as shown by the fronts of dimensionless mass at later times. In the scenario of $l = 1.0$ m, the rock matrix close to the injection well starts to reach equilibrium at 100 years. For the single-size-parallelepiped rock matrix, we can see the strong effect of anisotropy at early time and for

larger l values when comparing with the single-size-cube matrix case. For the four-size-cube rock matrix, the profiles are very different from those with single isotropic and anisotropic block cases because of slower diffusion with smaller rate coefficients for larger blocks of size $3l$ and $6l$. Even for $l=0.25$ m, there are no regions at equilibrium for the representative rock mass of the four blocks at 100 years of injection.

Figure 6d shows the relative effectiveness of $dsCO_2$ storage in the rock matrix in comparison with $scCO_2$ storage in fractures in fractured reservoirs. With time, the dominant $scCO_2$ storage in fractures is transitioned to the dominant $dsCO_2$ storage in the rock matrix when the minimum half-fracture spacing is relatively small. The ultimate ratio between $dsCO_2$ and $scCO_2$ mass stored in the fractured reservoirs depends on fracture and matrix porosity, the density of $scCO_2$ and brine, and $dsCO_2$ solubility in brine as shown in Eq. (15). It can also be seen that the dual-porosity model with the optimal rate coefficient underestimates the $dsCO_2$ storage over the 100 years because this model is only accurate for equilibrium conditions. Therefore, the numerical simulations with a dual-porosity model conducted by *Carneiro* [2009] may underestimate the significance of $dsCO_2$ storage in fractured reservoirs.

As demonstrated by the above two examples, it is important to take into account the anisotropy of matrix blocks because fracture spacing may be very different in three dimensions. It is also important to account for the multiple block sizes because fracture density varies significantly in the field. For large-scale GCS problems, early-time and late-time transfer regimes simultaneously occur in the different regions of the $scCO_2$ plume. This is very different from contamination and remediation problems where late-time behavior has been the focus of multi-rate diffusion and mass-transfer modeling. The developed approximate solutions can easily handle all these issues, and extend our modeling capabilities to include the anisotropy effect, the multi-rate effect, and the early- and late-time regimes.

4. Conclusions

Existing analytical and semi-analytical modeling of hydraulic, solute, and thermal diffusion processes in the subsurface have been focused on (1) isotropic matrix blocks and zones of low permeability with immobile fluid phases, and (2) truncation of sets of infinite series of exact analytical solutions by neglecting the early-time transfer regime. Following the exact solution forms of dimensionless mass, M_d, for small times for isotropic blocks available in the literature, we develop unified-form early- and late-time approximate solutions for various isotropic blocks (e.g., cylinders, spheres, slabs, square columns, and cubes) and anisotropic blocks (e.g., rectangular columns and parallelepipeds). The early-time solutions consist of a three-term polynomial function in terms of $\sqrt{T_d}$. The first coefficient depends only on the dimensionless area-to-volume ratio that is scaled by the minimum half-width or radius of blocks.

The last two coefficients are determined analytically for 1D diffusion in isotropic blocks, and are obtained by fitting the exact solutions of 2D and 3D diffusion and solely depend on the aspect ratios for anisotropic rectangular blocks. For the late-time solutions, only the leading exponential term is needed for isotropic blocks, while a few additional exponential terms are needed for highly anisotropic rectangular blocks. The optimal switchover T_d between the early- and late-time approximate solutions is determined to be between 0.157 and 0.229 for all blocks, with its highest relative approximation error less than 0.2%. For mass transfer by diffusion, it is found that (1) the early-time transfer regime is dominant, accounting for 50% to 88% cumulative mass gain/loss relative to the equilibrium ones, and (2) the degree of anisotropy in terms of aspect ratios has a significant impact on the fracture-matrix transfer.

Comparing our approximate solutions with conventional first-order dual-porosity and mobile-immobile fluid flow models indicates that the latter are inaccurate for both early- and late-time transfer regimes. The latter assumes a single matrix continuum with a capacity ratio of unity while the former honors the contribution of fast mass transfer occurring during the early-time regime to the late-time solutions and have a capacity ratio less than 1 determined analytically. The dual-porosity model with optimal rate coefficient can only accurately predict the diffusion timescale to reach equilibrium, while that with geometry-based rate coefficient produces an erroneous diffusion timescale.

The application of the developed approximate solutions to storage of $dsCO_2$ in an idealized fractured reservoir shows that the storage of $dsCO_2$ in the rock matrix is effective as long as the half-fracture spacing is less than 1 m for slab-like, cubical, and rectangular-parallelepiped matrix blocks at local scale. Calculations are performed for $scCO_2$ injection into a fractured reservoir with a 1D radial $scCO_2$ flow coupled with diffusive sinks of $dsCO_2$ from instantaneous dissolution at fracture-matrix interfaces. It is found that the ratio of the $dsCO_2$ mass stored in the rock matrix to the $scCO_2$ mass stored in the fractures can be as high as 2.2 when the minimum half-fracture spacing is relatively small in our considered cases. The ultimate value of this ratio depends on fracture and matrix porosity, the densities of $scCO_2$ and brine, and $dsCO_2$ solubility. It is also found that the effects of anisotropy and varying sizes of the matrix blocks are strong and cannot be neglected. The developed approximate solutions can easily extend our modeling capabilities to include the anisotropy effect, the multi-rate effect, and the early- and late-time regimes.

Acknowledgements

References

Aronofsky, J. S., L. Masse, and S. G. Natanson (1958), A model for the mechanism of oil recovery from the porous matrix due to water invasion in fractured reservoirs, *Soc. Petrol. Eng. J.*, 213(2), 2–4.

Barenblatt, G. E., I. P. Zheltov, and I. N. Kochina, (1960), Basic concepts in the theory of homogeneous liquids in fissured rocks, *Y. Aupl. Math. Mech. (USSR)*, 24(5), 1286-1303.

Becker, M. W., and R. J. Charbeneau (2000), First-passage-time transfer functions for groundwater tracer tests conducted in radially convergent flow, *J. Contam. Hydrol.*, 40, 299–310.

Birkholzer, J. T., C. M. Oldenburg, and Q. Zhou (2015), CO_2 migration and pressure evolution in deep saline aquifers, *Int. J. Greenh. Gas Control*, 40, 203–220, http://dx.doi.org/10.1016/j.ijggc.2015.03.022.

Brusseau, M. L., R. E. Jessup, and P. S. C. Rao (1989), Modeling the transport of solutes influenced by multiprocess nonequilibrium, *Water Resour. Res.*, 25(9), 1971–1988.

Carneiro, J. F. (2009), Numerical simulations on the influence of matrix diffusion to carbon sequestration in double porosity fissured aquifers, *Int. J. Greenh. Gas Control*, 3, 431–443.

Carrera, J., X. Sanchez-Vila, I. Benet, A. Medina, G. Galarza, and J. Guimera (1998), On matrix diffusion: Formulations, solution methods and qualitative effects, *Hydrogeol. J.*, 6(1), 178–190.

Carslaw, H. S., and J. C. Jaeger (1959), *Conduction of Heat in Solids,* 2nd Edition, Clarendon, Oxford.

Coats, K. H. (1989), Implicit compositional simulation of single-porosity and dual-porosity reservoirs, SPE 18427, presented at *10th SPE Symp. Reservoir Simulation*, Houston, Tex., Feb. 6-8.

Coats, K. H., and B. D. Smith (1964), Dead-end pore volume and dispersion in porous media, *Soc. Petrol. Eng. J.,* 4(1), 73–84, 1964.

Cortis, A., and J. T. Birkholzer (2008), Continuous time random walk analysis of solute transport in fractured porous media, *Water Resour. Res.,* 44, W06414, doi:10.1029/2007WR006596.

Crank, J. (1975), *The Mathematics of Diffusion*, 2nd ed., Oxford Univ. Press, New York, 1975.

Dykhuizen, R. C. (1990), A new coupling term for dual-porosity models, *Water Resour. Res.*, 26, 351-356, 1990.

Geiger, S., A. Cortis, and J. T. Birkholzer (2010), Upscaling solute transport in naturally fractured porous media with the continuous time random walk method, *Water Resour. Res.*, 46, W12530, doi:10.1029/2010WR009133.

Guan, J., F. J. Molz, Q. Zhou, H.-H. Liu, and C. Zheng (2008), Behavior of the mass transfer coefficient during the MADE-2 experiment: New insights, *Water Resour. Res.,* 44, W02423, doi:10.1029/2007WR006120.

Hadermann, J., and W. Heer (1996), The Grimsel (Switzerland) migration experiment: Integrating field experiments, laboratory investigations and modelling, *J. Contam. Hydrol.,* 21(1– 4), 87–100.

Haggerty, R., and S. M. Gorelick (1995), Multiple-rate mass transfer for modeling diffusion and surface reactions in media with pore-scale heterogeneity, *Water Resour. Res.,* 31(10), 2383-2400.

Haggerty, R., S. A. McKenna, and L. C. Meigs (2000), On the late-time behavior of tracer test breakthrough curves, *Water Resour. Res.,* 36(12), 3467-3479.

Haggerty, R., S. W. Fleming, L. C. Meigs, and S. A. McKenna (2001), Tracer tests in a fractured dolomite, 2, Analysis of mass transfer in singlewell injection-withdrawal tests, *Water Resour. Res.,* 37 (5), 1113–1128.

Haggerty, R., C. F. Harvey, C. F. von Schwerin, and L. Meigs, (2004), What controls the apparent timescale of solute mass transfer in aquifers and soils? A comparison of experimental results, *Water Resour. Res.,* 40, W01510, doi:10.1029/2002WR001716.

Holman, J. P. (1990), *Heat Transfer*, 7ed. McGraw-Hill, New York, N.Y.

Kazemi, H., L. Merrill, K. Porterheld, and P. Zeman (1976), Numerical simulation of water-oil

flow in naturally fractured reservoirs, *Soc. Petrol. Eng. J.*, 16(6), 317-326.

Lim, K. T., and K. Aziz (1995), Matrix-fracture transfer shape factors for dual-porosity simulators, *J. Petrol. Sci. Eng.,* 13, 169- 178.

Liu, G., C. Zheng, and S. M. Gorelick (2007), Evaluation of the applicability of the dual-domain mass transfer model in porous media containing connected high-conductivity channels, *Water Resour. Res.,* 43, 725-732.

Maloszewski, P., and A. Zuber (1985), On the theory of tracer experiments in fissured rocks with a porous matrix, *J. Hydrol.,* 79, 333–358.

Maloszewski, P., and A. Zuber (1990), Mathematical modeling of tracer behavior in short-term experiments in fissured rocks, *Water Resour. Res.,* 26 (7), 1517–1528.

Maloszewski, P., and A. Zuber, (1993), Tracer experiments in fractured rocks: Matrix diffusion and the validity of models, *Water Resour. Res.*, 29(8), 2723–2735.

March, R., F. Doster, and S. Geiger (2016), Accurate early-time and late-time modeling of countercurrent spontaneous imbibition, *Water Resour. Res.*, 52, doi:10.1002/2015WR018456.

McWhorter, D. B., and D. K. Sunada (1990), Exact integral solutions for two-phase flow, *Water Resour. Res.*, 26(3), 399–413.

Meigs, L. C., and R. L. Beauheim (2001), Tracer tests in a fractured dolomite, 1. Experimental design and observed tracer recoveries, *Water Resour. Res.,* 37 (5), 1113–1128.

Moench, A. F. (1995), Convergent radial dispersion in a double-porosity aquifer with fracture skin: analytical solution and application to a field experiment in fractured chalk, *Water Resour. Res.*, 31 (8), 1823–1835.

Novakowski, K. S., G. Bickerton, and P. Lapcevic (2004), Interpretation of injection–withdrawal tracer experiments conducted between two wells in a large single fracture, *J. Contam. Hydrol.,* 73, 227–247.

Reimus, P., G. Pohll, T. Mihevc, J. Chapman, M. Haga, B. Lyles, S. Kosinski, R. Niswonger, and P. Sanders (2003), Testing and parameterizing a conceptual model for solute transport in a fractured granite using multiple tracers in a forced-gradient test, *Water Resour. Res.,* 39(12), 1356. doi:10.1029/2002WR001597.

Silva, O. J. Carrera, M. Dentz, S. Kumar, A. Alcolea, and M. Willmann (2009), A general real-time formulation for multi-rate mass transfer problems, *Hydrol. Earth Syst. Sci.,* 13, 1399–1411.

Silva, O. and J. Carrera (2008), mod_process_MRMT.f90, A Fortran Module to Include Multi-Rate Mass Transfer like Processes, User's guide, Institute of Environmental Diagnosis and Water Studies, Barcelona, Spain.

Spycher, N., K. Pruess, and J. Ennis-King (2003), CO_2–H_2O mixtures in the geological sequestration of CO_2 . I. Assessment and calculation of mutual solubilities from 12 to 100 °C and up to 600 bar, *Geochim. Cosmochim. Acta* 67 (16), 3015–3031.

Spycher, N., and K. Pruess (2005), CO_2–H_2O mixtures in the geological sequestration of CO_2. II. Partitioning in chloride brines at 12–100 °C and up to 600 bar, *Geochim. Cosmochim. Acta* 69 (13), 3309–3320.

Sudicky, E.A., and E. O. Frind (1982), Contaminant transport in fractured porous media: analytical solutions for a system of parallel fractures, *Water Resour. Res.*, 18 (7), 1634–1642.

Tang, D. H., E. O. Frind, and E. A. Sudicky (1981), Contaminant transport in fractured porous media: analytical solution for a single fracture, *Water Resour. Res.*, 17 (3), 555–564.

Tecklenburg, J., I. Neuweiler, J. Carrera, and M. Dentz (2016), Multi-rate mass transfer modeling of two-phase flow in highly heterogeneous fractured and porous media, *Adv. Water Resour.*, 91, 63-77, DOI: 10.1016/j.advwatres.2016.02.010.

Tecklenburg, J., I. Neuweiler, M. Dentz, J. Carrera, S. Geiger, C. Abramowski, and O. Silva (2013), A non-local two-phase flow model for immiscible displacement in highly heterogeneous porous media and its parametrization, *Adv. Water Resour.* 62, 475-485.

USDOE (US Department of Energy) (2008), *Carbon sequestration atlas of the United States and Canada*, 2nd Edn. National Energy Technology Laboratory, Pittsburgh, PA, USA.

van Genuchten, M. T., and P. J. Wierenga (1976), Mass transfer studies in sorbing porous media, 1, Analytical solutions, *Soil Sci. Soc. Am. J.*, 40(4), 473–480.

Warren, J. P., and P. J. Root (1963), The behavior of naturally fractured reservoirs, *Soc. Petrol. Eng. J.*, 3(3), 244–255.

Willmann, M., J. Carrera, and X. Sánchez-Vila (2008), Transport upscaling in heterogeneous aquifers: what physical parameters control memory functions? *Water Resour. Res.*, 44, W12437, doi:10.1029/2007WR006531.

Zhang, Y., L. Pan, K. Pruess, and S. Finsterle (2011), A time-convolution approach for modeling heat exchange between a wellbore and surrounding formation, *Geothermics,* 40, 261–266.

Zhou, Q., H.-H. Liu, G. S. Bodvarsson, and F. J. Molz (2006), Evidence of multi-process matrix diffusion in a single fracture from a field tracer test, *Transport Porous Med.,* 63(3), 473–487.

Zhou, Q., H.-H. Liu, F. J. Molz, Y. Zhang, and G. S. Bodvarsson (2007), Field-scale effective matrix diffusion coefficient for fractured rock: Results from literature survey, *J. Contam. Hydrol.*, 93, 161 – 187, doi:10.1016/j.jconhyd. 2007. 02.002.

Zhou Q, J. T. Birkholzer, C. -F. Tsang and J. Rutqvist (2008), A method for quick assessment of CO_2 storage capacity in closed and semi-closed saline formations, *Int. J. Greenh. Gas*

Control, 2(4), 626–639.

Zhou, Q., J. T. Birkholzer, and C.-F. Tsang (2009), A semi-analytical solution for large-scale injection-induced pressure perturbation and leakage in a laterally bounded aquifer-aquitard system, *Transport Porous Med.* 78(1), 127-148.

Zhou Q, J. T. Birkholzer, E. Mehnert, Y. F. Lin and K. Zhang (2010), Modeling basin- and plume-scale processes of CO_2 storage for full-scale deployment, *Ground Water* 48(4), 494–514.

Zimmerman, R. W., G. Chen, T. Hadgu, and G. S. Bodvarsson (1993), A numerical dual-porosity model with semianalytical treatment of fracture/matrix flow, *Water Resour. Res.*, 29(7), 2127–2137, doi:10.1029/93WR00749.

Table 1. Solution coefficients, the switchover dimensionless time, the maximum relative error (ε_{max}) at T_{d0}, the dimensionless mass at T_{d0}, N for late-time solutions, and the dimensionless area-to-volume ratio (R) for the approximate solutions for different shapes of a matrix block.
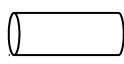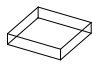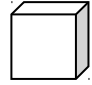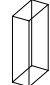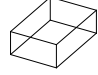
Block Shape	Sphere	Cylinder	Slab	Square Column	Cube	Rectang. Column	Rectang. Box
a_1	$6/\sqrt{\pi}$	$4/\sqrt{\pi}$	$2/\sqrt{\pi}$	$4/\sqrt{\pi}$	$6/\sqrt{\pi}$	$2R/\sqrt{\pi}$	$2R/\sqrt{\pi}$
a_2	-3	-0.9608	0	-1.2735	-3.8171	Eq. (7a)	Eq. (9b)
a_3	0	-0.3832	0	0	1.4232	0	Eq. (9c)
b_1	$6/\pi^2$	$4/\beta_1^2$	$8/\pi^2$	$\frac{8}{\pi^2}$	$\frac{8}{\pi^2}$	Eq. (7b)	Eq. (9d)
b_2	π^2	β_1^2	$\pi^2/4$	$2\pi^2/4$	$3\pi^2/4$	Eq. (7c)	Eq. (9e)
N	1	1	1	1	1	1-39	1-59
T_{d0}	0.157	0.192	0.213	0.215	0.229	0.22	0.22
ε_{max} (%)	0.034	0.100	0.153	0.083	0.040	0.073-0.164	0.001-0.123
M_{d0}	0.871	0.772	0.521	0.772	0.902	0.50-0.75	0.50-0.88
R	3	2	1	2	3	$1+R_{ly}^{\square}$	$1+R_{ly}+l$

Figure 1. (a) Solutions of time-dependent dimensionless mass with finite terms (N = 1, 10, 25, 50, 100, 1000) in the infinite series solutions in Eq. (3), with symbols denoting the solutions (M_{dN} , T_{dN}) beyond whose T_d faster-diffusion terms are negligible, (b) relative errors (%) of the solutions with Eq. (5), Eq. (5a), and Eq. (5b) in comparison to their exact solutions, with black symbols denoting T_{d0} points, (c) comparison of the approximate solutions, Eq. (5), with their corresponding exact solutions (with N = 1000 or 150 finite terms) and their leading-term solutions (N = 1), with large symbols denoting the switchover dimensionless time, and (d) exact solution of relative concentration as a function of distance from the block center, for spherical (black solid lines) and slab-like (red dashed lines) blocks, with labels for dimensionless time.

Figure 2. (a) Comparison between the approximate solutions (in symbols) and the exact solutions (in solid lines) and (b) coefficient a_2 and N for a rectangular-column block, as a function of the aspect ratio R_{ly} , and (c) comparison between the approximate solutions (in black symbols) and the exact solutions (in black solid lines) for a rectangular-parallelepiped block, as a function of the aspect ratios R_{ly} and R_{lz} . Also shown is the comparison (in red symbols and solid lines) for isotropic slab-like, square-column, and cubical blocks. (d) Comparison of the approximate solutions for an isotropic block of slab-like, cylindrical, spherical, square-column, or cubical shapes.

Figure 3. (a) Coefficient a_2 and (b) a_3 of the early-time approximate solutions, and (c) the relative error between the early-time approximate and exact solutions at T_{d0} , and (d) the number of exponential terms (N) needed in the late-time approximate solutions, as functions of aspect ratios R_{ly} and R_{lz} , for a rectangular-parallelepiped block. Symbols denote data points of (R_{ly} , R_{lz}) pairs for the contours.

Figure 4. Comparison of the approximate solutions to two first-order dual-porosity models with geometric-based and optimal rate coefficients for a slab-like and cubical block.

Figure 5. Contours of the dimensionless mass as functions of time and half-fracture spacing for (a) slabs, (b) cubes, and (c) anisotropic rectangular parallelepipeds with $R_{ly}=0.5$ and $R_{lz}=0.2$, and (d) comparison of the time-dependent dimensionless mass for single- and multiple-size cubes and single-size anisotropic rectangular parallelepipeds with $l=0.25, 0.5, 1$ m.

Figure 6. Profiles of dsCO$_2$ dimensionless mass at 5, 25, 50, 75 and 100 years in the rock matrix with (a) single-size cubes, (b) four-size cubes, and (c) single-size anisotropic rectangular parallelepipeds with $R_{ly}=0.5$ and $R_{lz}=0.2$, with the minimum half-fracture spacing of 0.25, 0.50, and 1.0 m, and (d) comparison of the time-dependent ratio between the dsCO$_2$ mass

stored in the rock matrix and the scCO$_2$ mass stored in the fractures for all the nine scenarios, as well as the dual-porosity model with optimal rate coefficient for the multi-cube case with $l=1.0$ m.